

## **Fabrication of highly n-type-doped germanium nanowires and Ohmic contacts using ion implantation and flash lamp annealing**

Echresh, A.; Prucnal, S.; Li, Z.; Hübner, R.; Ganss, F.; Steuer, O.; Bärwolf, F.; Jazavandi Ghamsari, S.; Helm, M.; Zhou, S.; Erbe, A.; Rebohle, L.; Georgiev, Y.;

Originally published:

November 2022

**ACS Applied Electronic Materials 4(2022), 5256-5266**

DOI: <https://doi.org/10.1021/acsaelm.2c00952>

Perma-Link to Publication Repository of HZDR:

<https://www.hzdr.de/publications/Publ-36230>

Release of the secondary publication  
on the basis of the German Copyright Law § 38 Section 4.

# Fabrication of highly n-type-doped germanium nanowires and Ohmic contacts using ion implantation and flash lamp annealing

Ahmad Echresh,<sup>\*,†,‡</sup> Slawomir Prucnal,<sup>†</sup> Zichao Li,<sup>†</sup> René Hübner,<sup>†</sup> Fabian Ganss,<sup>†</sup> Oliver Steuer,<sup>†</sup> Florian Bärwolf,<sup>¶</sup> Shima Jazavandi Ghamsari,<sup>†</sup> Manfred Helm,<sup>†,‡</sup> Shengqiang Zhou,<sup>†</sup> Artur Erbe,<sup>†,§</sup> Lars Rebohle,<sup>†</sup> and Yordan M. Georgiev<sup>\*,†,||</sup>

<sup>†</sup>*Institute of Ion Beam Physics and Materials Research, Helmholtz-Zentrum  
Dresden-Rossendorf (HZDR), 01328 Dresden, Germany*

<sup>‡</sup>*Institute of Applied Physics, Technical University of Dresden, 01062 Dresden, Germany*

<sup>¶</sup>*IHP–Leibniz-Institut für innovative Mikroelektronik, Im Technologiepark 25, 15236  
Frankfurt (Oder), Germany*

<sup>§</sup>*Center for Advancing Electronics Dresden (CFAED), Technical University of Dresden,  
01062 Dresden, Germany*

<sup>||</sup>*Institute of Electronics at the Bulgarian Academy of Sciences, 72, Tsarigradsko Chausse  
Blvd., 1784 Sofia, Bulgaria*

E-mail: a.echresh@hzdr.de; y.georgiev@hzdr.de

## Abstract

Accurate control of doping and fabrication of metal contacts on n-type germanium nanowires (GeNWs) with low resistance and linear characteristics remain a major challenge in germanium-based nanoelectronics. Here, we present a combined approach to

fabricate Ohmic contacts on n-type-doped GeNWs. Phosphorus (P) implantation followed by millisecond rear-side flash lamp annealing was used to produce highly n-type-doped Ge with an electron concentration in the order of  $10^{19} - 10^{20} \text{ cm}^{-3}$ . Electron beam lithography, inductively coupled plasma reactive ion etching, and nickel (Ni) deposition were used to fabricate GeNW-based devices with symmetric Hall bar configuration, which allows detailed electrical characterization of the NWs. Afterward, rear-side flash lamp annealing was applied to form Ni germanide at the Ni-GeNWs contacts to reduce the Schottky barrier height. The two-probe current-voltage measurements on n-type-doped GeNWs exhibit linear Ohmic behavior. Also, the size-dependent electrical measurements showed that carrier scattering near the NW surfaces and reduction of the effective NW cross-section dominate the charge transport in the GeNWs.

**Keywords:** Germanium nanowires; ion implantation; flash lamp annealing; n-type-doped; Ohmic contacts; Hall bar configuration.

## Introduction

Germanium (Ge) is the most compatible semiconductor material with silicon (Si)-based complementary metal-oxide semiconductor (CMOS) processes. Also, Ge is a promising candidate for next-generation high-mobility devices because of its higher electron and hole mobility compared to Si, which leads to an improved device performance.<sup>1,2</sup> On the other hand, nanowires (NWs) have been considered as an attractive building block for electronic and optoelectronic devices because of their unique properties, such as low dimensionality, quantum confinement, surface sensitivity, and low leakage current.<sup>3-6</sup> Hence, GeNWs are promising high-mobility nanostructures for future nanoelectronics. Monolithic integration of high-mobility semiconductor materials with Si technology is a key milestone for the next generation of high-performance nanoelectronic devices. Therefore, Ge would need p-type and n-type doping with high carrier densities to integrate with Si as a primary material in

nanoelectronic devices.<sup>7</sup> There are a number of challenges, which need to be addressed for facilitating this integration.

The achievable doping levels in n-type Ge are lower than those in p-type Ge. Also, accurate control of doping is quite challenging for NW-based devices.<sup>8-14</sup> So far, there have been several investigations regarding the control of the dopant depth as well as dopant concentration, which led to the development of different doping techniques.<sup>15-19</sup> A non-destructive dopant in-diffusion process was used to dope phosphorus and arsenic into the top-down fabricated GeNWs with active doping levels in the range of  $10^{19} \text{ cm}^{-3}$ .<sup>16</sup> Monolayer doping (MLD) method was reported for phosphorus doping into SiNWs with a high surface concentration in the order of  $10^{20} \text{ cm}^{-3}$ .<sup>17</sup> M. S. Seifne et al. reported p-type doped GeNWs with the homogeneous incorporation of gallium with an estimated carrier concentration of  $5 \times 10^{20} \text{ cm}^{-3}$ .<sup>10</sup> Y. Berencén et al. presented the phosphorus and boron doping of individual drop-casted Si/SiO<sub>2</sub> core/shell NWs using ion implantation.<sup>19</sup> In comparison to other doping methods, ion implantation demonstrates several advantages including high efficiency, high reproducibility, and precise control of the concentration and the depth profile of the dopants. In addition, ion implantation can provide a good homogeneity of the dopant depth distribution using one- or multiple-shot implantation, depending on the desired depth profile.<sup>7,19,20</sup> However, ion implantation is a destructive method, which leads to the amorphization of the lattice structure. Therefore, an annealing process is needed to restore the lattice order and activate the dopant atoms.<sup>21</sup>

In addition, it is quite tricky to fabricate Ohmic contacts on n-type Ge because of Fermi level pinning (FLP) at the metal-semiconductor interfaces, which leads to a large Schottky barrier height (SBH).<sup>22-25</sup> The interface states pin the Fermi level and make the SBH independent of the metal work function.<sup>26,27</sup> Covalent semiconductors such as bulk Ge have a large number of dangling bonds at the surface, which introduce energy levels in the band-gap similar to those of acceptor impurities. If the density of surface states is sufficiently large, the Fermi level will be pinned close to the valence band and form the Schottky barrier.<sup>28,29</sup>

One way to achieve Ohmic contacts for n-type semiconductors is by having a heavily doped thin layer at the metal-semiconductor interface. This leads to a very thin depletion region, through which field emission can take place.<sup>27</sup> K. Gallacher et al. reported that the Schottky barrier width is inversely proportional to the doping density in semiconductors and the width is thin enough to allow quantum mechanical tunneling for doping densities higher than  $10^{19} \text{ cm}^{-3}$ .<sup>30</sup> Also, it has been reported that inserting an intermediate layer into the interface can decrease the FLP and allows changing the barrier by choosing a metal with a different work function.<sup>26,31,32</sup> Moreover, introducing nickel germanide with a stoichiometric compound (NiGe) at the metal-semiconductor interface can reduce the SBH.<sup>30,33,34</sup> A low resistance Ni Ohmic contacts on the highly n-type  $\text{Ge}_{1-x}\text{Sn}_x$  layer was reported using the Ni germanide formation.<sup>35,36</sup>

The small size and large surface-to-volume ratio of GeNWs might lead to a change in the band-gap and induce more surface states in the band-gap, respectively, in comparison to bulk Ge. Therefore, interfacial phenomena such as FLP can show dramatic differences compared to planar devices.<sup>37,38</sup> It was reported that the FLP in nanoscale devices can result in SBH larger than that at the corresponding bulk interface.<sup>39</sup> S. Sett et al. reported the formation of Cr/Au contacts on the single GeNWs, grown using Au catalyst from vapor, with a low SBH in the range of 0.15 to 0.3 eV.<sup>40</sup> Vertical phosphorus-doped GeNWs, grown using vapor-liquid-solid epitaxy, were reported with Ni-Ge Schottky contacts with SBH of 0.3-0.4 eV.<sup>41</sup> Recently, a promising approach regarding the fabrication of high-quality contacts such as Cu and Al on semiconductors using in-situ Joule heating in a transmission electron microscope was presented, which creates very sharp and well defined one-dimensional contacts between a metal and a semiconductor.<sup>42,43</sup> Although this method delivering very good results, it is not industrially relevant. Despite all of these investigations, so far, the fabrication of appropriate Ohmic contacts on the n-type-doped GeNWs is quite challenging and requires more comprehensive investigations.

In this work, we report on a combined approach to fabricate Ohmic contacts on n-type-

doped GeNWs. To have precise control over dopant concentrations and their depth profile, first, phosphorus (P) atoms were implanted into the Ge layer using ion beam implantation. Subsequently, an advanced annealing process, rear-side flash lamp annealing (rFLA), which takes place in a timescale of 100  $\mu\text{s}$  to 100 ms and operates far from thermal equilibrium, was performed to activate the P atoms and recrystallize the Ge layer, which is amorphized during implantation. Highly n-type-doped Ge layers with effective carrier concentrations in the order of  $10^{19} - 10^{20} \text{ cm}^{-3}$  were achieved. Then, GeNWs with different widths were fabricated in the n-type-doped Ge layers using electron beam lithography (EBL) and inductively coupled plasma reactive ion etching (ICP-RIE). Nickel contacts were deposited in a symmetric six-contact Hall bar configuration, which facilitates the Hall effect and four-probe measurements simultaneously. To improve the linear characteristics of the Ni-GeNWs contacts, a second rFLA was applied to induce Ni germanide formation at the Ni-Ge interface, reducing the SBH. Furthermore, the effect of NW width on transport parameters such as resistivity ( $\rho$ ) and Hall carrier mobility ( $\mu_H$ ) was investigated.

## Experiments

### Phosphorus doping of GeOI substrates

Most semiconductor-based devices have at least one junction between p-type and n-type semiconductors. Hence, to facilitate the fabrication of axial p–n junctions along the GeNWs for optoelectronic devices, p-type ( $\sim 10^{20} \text{ cm}^{-3}$ ) germanium-on-insulator (GeOI) substrates with a 38-nm-thick top Ge layer,  $2.1 \times 10^{-3} (\Omega \cdot \text{cm})$  resistivity, and 200 nm buried  $\text{SiO}_2$  layer were used in this study. The substrates were implanted with P ions with an energy of 15 keV and two different fluences, as mentioned in Table 1, to convert the highly p-type Ge layer to a highly n-type semiconductor. To prevent the Ge surface from roughening and sputtering during ion implantation,<sup>44,45</sup> a 15-nm-thick amorphous silicon (a-Si) capping layer was deposited using a *Nordiko* 2000 sputter deposition tool. After ion implantation, the a-Si

capping layer was removed using tetramethylammonium hydroxide (TMAH, 25%) solution at 60 °C.<sup>46</sup> Then, the P-implanted samples were annealed using rFLA with an optimized energy density of 125 Jcm<sup>-2</sup> for 20 ms to recrystallize the amorphous Ge layer induced by the ion implantation and to activate the P dopant atoms. The rFLA process is described in detail elsewhere.<sup>7</sup>

Table 1: Ion implantation parameters, P concentration, carrier concentration obtained using van-der-Pauw configuration, and the conducting type of un-implanted and P-doped samples.

Sample	energy (keV)	fluence (cm <sup>-2</sup> )	P con. (cm <sup>-3</sup> )	carrier con. (cm <sup>-3</sup> )	type
GeOI-0	-	-	-	$1.3 \times 10^{20}$	p
GeOI-1	15	$5 \times 10^{15}$	$2.0 \times 10^{21}$	$5.8 \times 10^{19}$	n
GeOI-2	15	$7.5 \times 10^{15}$	$3.1 \times 10^{21}$	$1.4 \times 10^{20}$	n

Rutherford backscattering spectrometry (RBS) was performed to investigate the crystal quality of the samples in the un-implanted, as-implanted, and annealed stages. The RBS measurements were conducted using the 1.7 MeV  $He^+$  beam with a diameter of 1 mm at the 2 MeV van de Graaf accelerator at the Ion Beam Center of the Helmholtz-Zentrum Dresden-Rossendorf. Secondary ion mass spectrometry (SIMS) measurements were done to determine the P dopant atoms distribution in the Ge matrix using an *IONTOF V* tool, with cesium sputtering at 500 eV impact energy, a raster size of 300×300  $\mu m$  in negative mode, and an analyzing Bi ion beam of 25 keV with a raster size of 100×100  $\mu m$ . The induced strain in the P-doped Ge layers was investigated by high-resolution X-ray diffraction (HR-XRD). The XRD was performed with a *Rigaku SmartLab* diffractometer with a Cu K $_{\alpha 1}$  radiation source. Moreover, the crystal quality of the P-implanted Ge layers was studied by micro-Raman spectroscopy in backscattering geometry in the range of 100 to 600 cm<sup>-1</sup> using a green (532 nm) *Nd:YAG* laser with a liquid-nitrogen-cooled charge-coupled device camera. The electrical characterization of the GeOI substrates was carried out using a commercial *Lakeshore* system with van-der-Pauw configuration via silver wire-bonding. Also, a superconducting magnet with fields up to  $\pm 4$  T was used.

## Fabrication of phosphorus-doped GeNWs

The GeOI-1 substrate, P-implanted with the energy of 15 keV and a fluence of  $5 \times 10^{15} \text{ cm}^{-2}$ , was patterned using EBL and ICP-RIE to fabricate n-type-doped GeNWs with different widths as follows. The negative tone resist hydrogen silsesquioxane (HSQ) (*Dow Corning X-1541* with original 6% concentration), which has sub-5 nm resolution, small edge roughness, and high etch resistance,<sup>47–49</sup> was diluted to 2% concentration in methyl isobutyl ketone (MIBK) and spin-coated on the pre-cleaned and passivated<sup>50</sup> GeOI substrates at 2000 rpm for 30 s to get a 40-nm-thick HSQ layer. Then, the samples were baked at 120 °C for 2 min and immediately loaded into the EBL system. The electron beam exposure was carried out using a *Raith e-Line Plus* system at an accelerating voltage of 10 kV,  $1000 \mu\text{Ccm}^{-2}$  area dose,  $30 \mu\text{m}$  aperture size, and 2 nm area step size. The samples were developed using a high-contrast TMAH-based development process<sup>51</sup> and dried with an N<sub>2</sub> gun. A *SENTECH* ICP-Reactive Ion Etcher SI 500 with a continuous flow of SF<sub>6</sub> (10 sccm), C<sub>4</sub>F<sub>8</sub> (22 sccm), and O<sub>2</sub> (5 sccm) gases at 0.9 Pa chamber pressure, 400 W ICP power, and 12 W RF power was used to transfer the HSQ patterns of the NWs into the Ge layer anisotropically. In the end, the HSQ was removed by a dip in HF (1% in H<sub>2</sub>O) solution for 50 s at room temperature. In order to fabricate the metal contacts, EBL, metal deposition, and lift-off processes were employed. A positive tone resist, polymethyl methacrylate (PMMA), was spin-coated on the samples with the patterned GeNWs at 3000 rpm for 50 s and baked at 180 °C for 10 min. Then, the electron beam exposure was performed using the following parameters: 10 kV accelerating voltage,  $100 \mu\text{Ccm}^{-2}$  area dose,  $30 \mu\text{m}$  aperture size, and 20 nm area step size. The exposed samples were developed in isopropanol/deionized water (7:3) solution. Right before nickel (Ni) deposition for the metal contacts, samples were put into an acetic acid/deionized water (1:7) solution to remove the native oxide.<sup>50</sup> An ultrahigh vacuum electron beam *Bestec* evaporation tool was used to deposit a 70-nm-thick layer of Ni. In the end, the lift-off was carried out in acetone. Two- and four-probe measurements were done on the GeNWs to examine the Ni-GeNWs contacts and the NWs resistance. Since the two-

probe current–voltage characteristics were not perfectly linear, an rFLA was performed to improve the Ni-GeNWs contacts and reduce the contact resistance. Afterward, the electrical characteristics were investigated using two-probe, four-probe, and Hall effect measurements.

Scanning electron microscopy (SEM) imaging was done using the *Raith e-Line Plus* system. To investigate the structural properties of the n-type-doped GeNWs, cross-sectional bright-field and high-resolution transmission electron microscopy (TEM) were performed with an image- $C_s$ -corrected Titan 80-300 (FEI) microscope operated at an accelerating voltage of 300 kV. High-angle annular dark-field (HAADF) scanning transmission electron microscopy (STEM) imaging and spectrum imaging analysis based on energy-dispersive X-ray spectroscopy (EDXS) were performed at 200 kV with a *Talos F200X* microscope equipped with a *Super-X* EDXS detector system (FEI). All electrical measurements of n-type-doped GeNWs were carried out in vacuum ( $<10^{-7}$  mbar) using a semiconductor parameter analyzer (*Agilent*, 4156C) via four needle tips. Also, a superconducting magnet with fields up to  $\pm 2$  T were used to perform the Hall effect measurements.

## Results and discussion

### Characterization of phosphorus-doped Ge layers

#### RBS and SIMS measurements

The crystalline structure of the P-implanted Ge layer was investigated using RBS, performed in random (R) and channeling (C) backscattering directions. The RBS spectra of the Ge signal for un-implanted (GeOI-0), as-implanted (GeOI-1, as-imp.), and annealed (GeOI-1, rFLA) samples are shown in Figure 1(a). The high channeling backscattering yield of the as-implanted GeOI-1 sample is related to the amorphization of the Ge layer. The minimum yield ( $\chi_{min}$ ) of the Ge signal, which is defined as a ratio of integrated channeling yield to random yield (i.e. channeling yield/random yield), was 0.358 (un-implanted), 0.654 (as-

implanted), and 0.361 (rFLA). The  $\chi_{min}$  of the annealed GeOI-1 sample is very close to the  $\chi_{min}$  of the GeOI-0 sample, indicating good recrystallization of the Ge layer via solid phase epitaxial regrowth during rFLA.<sup>7</sup>

Moreover, SIMS was used to determine the depth profile of the P dopant atoms in the Ge matrix of the GeOI-1 sample before and after rFLA, shown in Figure 1(b). As can be seen, there is a slight redistribution of P atoms across the Ge layer after rFLA with an accumulation of P at the Ge surface and Ge/SiO<sub>2</sub> interface.

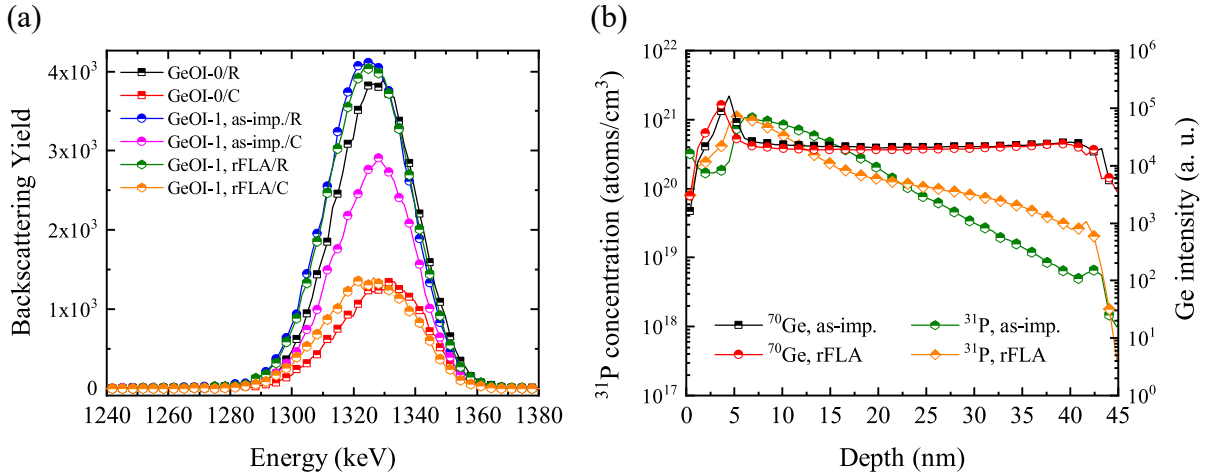


Figure 1: (a) RBS random (R) and channeling (C) backscattering yield spectra of GeOI-0, as-implanted and annealed GeOI-1 samples. (b) SIMS measurements of the P distribution in the Ge layer of the GeOI-1 sample before and after rFLA.

## X-ray diffraction

High-resolution X-ray diffraction (HR-XRD) measurements were performed along the (004) and (224) reflections to determine the out-of-plane ( $a^\perp$ ) and in-plane ( $a^\parallel$ ) lattice parameters of the Ge layers of the GeOI-0 (un-implanted), GeOI-1 (rFLA) and GeOI-2 (rFLA) samples, respectively. The symmetric 004 and asymmetric 224 diffraction peaks of the un-implanted and P-doped (after rFLA) Ge layers are shown in Figure 2(a,b) and summarized in Table 2. The  $a^\perp$  of GeOI-0 sample is 5.660 Å, while  $a^\parallel$  is 5.656 Å. The lattice parameter of relaxed bulk Ge ( $a^{\text{bulk}}$ ) is 5.657 Å.<sup>52</sup> Hence, the un-implanted sample (GeOI-0) exhibits a slight out-

of-plane tensile strain. A detailed calculation of the lattice parameters  $a^\perp$  and  $a^\parallel$  is provided in the Supporting Information and summarized in Table 2. As seen, P implantation leads to a contraction of the lattice. Since the covalent radius of P (107 pm) is smaller than that of Ge (120 pm), P can efficiently reduce the lattice parameters of the P-doped Ge layers.<sup>53,54</sup> As seen, P doping in the GeOI-1 sample leads to compensation for the already existing out-

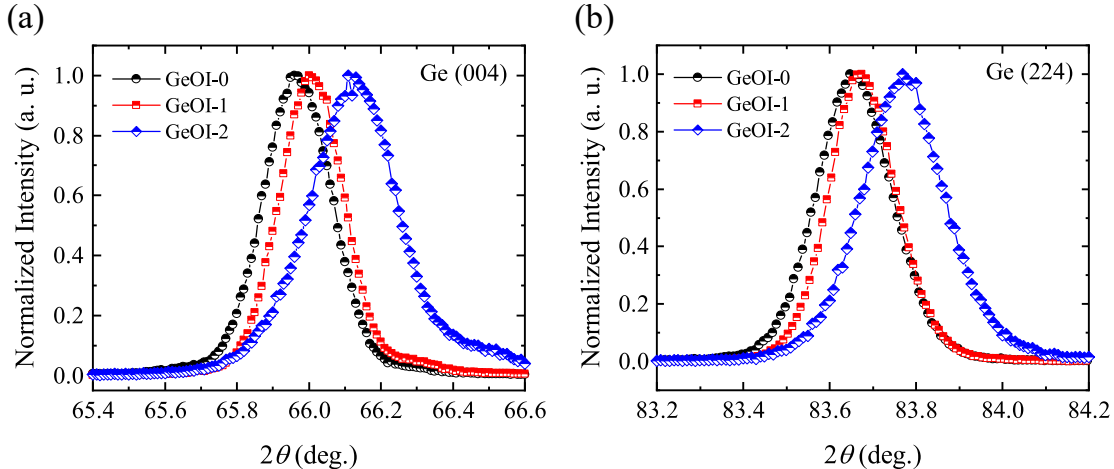


Figure 2: X-ray diffraction pattern of (a) symmetric (004) and (b) asymmetric (224) reflections of Ge layer of the GeOI-0 (un-implanted), GeOI-1 (rFLA) and GeOI-2 (rFLA) samples.

of-plane tensile strain. The incorporation of more P dopants in the GeOI-2 sample gives rise to out-of-plane compressive strain in the Ge layer. Also, the full width at half maximum (FWHM) of 004 and 224 diffraction peaks of the GeOI-2 sample is slightly wider than the one of the GeOI-1 sample, which is related to the higher fluence of P implantation, leading to lower crystal quality after rFLA compared to the GeOI-1 sample.

Table 2: Symmetric 004, asymmetric 224 diffraction peak positions, out-of-plane ( $a^\perp$ ) and in-plane ( $a^\parallel$ ) parameters, out-of-plane strain ( $\epsilon^\perp$ ) and in-plane strain ( $\epsilon^\parallel$ ) of the Ge layers of the GeOI-0 (un-implanted), GeOI-1 (rFLA) and GeOI-2 (rFLA) samples.

Sample	$2\theta_{(004)}$ ( $^\circ$ )	$2\theta_{(224)}$ ( $^\circ$ )	$a^\perp$ ( $\text{\AA}$ )	$a^\parallel$ ( $\text{\AA}$ )	$\epsilon^\perp$ (%)	$\epsilon^\parallel$ (%)
GeOI-0	65.96	83.65	5.660	5.656	+0.06	-0.01
GeOI-1	66.00	83.67	5.657	5.658	0.00	+0.02
GeOI-2	66.11	83.77	5.649	5.659	-0.14	+0.04

## Raman spectroscopy

To study the influence of P doping on the optical phonon mode of the Ge layer, micro-Raman spectroscopy measurements were performed at room temperature. The normalized Raman spectra of the un-implanted, as-implanted, and annealed samples are shown in Figures 3(a) and 3(b). The sharp peak of the un-implanted sample (GeOI-0), located at  $299.7 \text{ cm}^{-1}$ , is related to the transverse/longitudinal optical (TO/LO) phonon mode of crystalline Ge (c-Ge). The optical phonon mode of c-Ge in relaxed Ge is located at  $300.5 \text{ cm}^{-1}$ .<sup>54</sup> The as-implanted GeOI-1 and GeOI-2 samples show a broad peak centered at around  $272 \text{ cm}^{-1}$  in addition to the intense peak of the TO phonon mode of c-Ge, as shown in Figure 3(a). This broad peak is related to the amorphous Ge (a-Ge) layer induced by the P implantation. The intensity of the amorphous peak increases by raising the implantation fluence. The narrow peak is attributed to a phonon signal coming from the crystalline part of the Ge layer under the amorphized Ge, which can act as a seed layer for recrystallization via solid phase epitaxial regrowth during rFLA.<sup>7</sup>

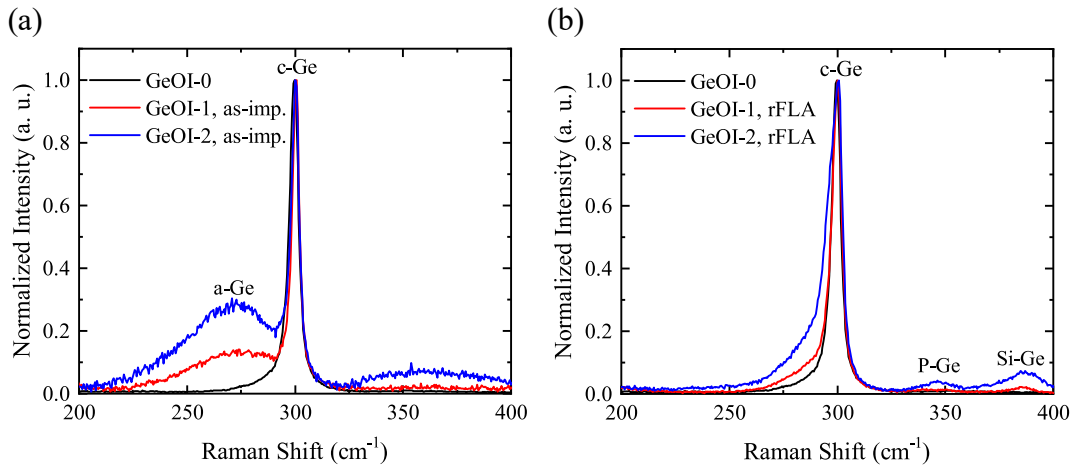


Figure 3: Normalized micro-Raman spectra of un-implanted, as-implanted (a) and rFLA (b) samples.

The Raman spectra of the annealed GeOI-1 and GeOI-2 samples are shown in Figure 3(b). The broad peak, related to a-Ge, disappeared after rFLA. The TO phonon mode of c-Ge for the annealed GeOI-1 and GeOI-2 samples is located at  $300.2 \text{ cm}^{-1}$  and  $300.4 \text{ cm}^{-1}$

, respectively. The blue-shift of the TO phonon mode of c-Ge with respect to the un-implanted sample, GeOI-0, can be related to the alloy disorder and induced strain in the Ge lattice because of P incorporation.<sup>52,54</sup> The first weak broad peak at about  $346.6 \text{ cm}^{-1}$  can be assigned to the local vibrational phonon mode of P-Ge in the Ge matrix, which indicates P dopant atoms were placed into the substitutional sites in the crystalline region of the Ge lattice.<sup>55</sup> The other broad peak, centered at  $386.3 \text{ cm}^{-1}$ , is related to the local vibrational phonon mode of Si-Ge.<sup>56</sup> The SiGe layer is formed close to the surface because of Si penetration from the a-Si capping layer into the Ge surface during ion implantation. As seen, the intensity of the P-Ge broad peak increased by increasing the P implantation fluence because of the higher incorporation of P atoms in the Ge matrix.

The TO phonon mode of c-Ge is asymmetrically broadened toward lower wavenumbers, which can be related to a Fano interference.<sup>55,57</sup> The Fano interference occurs because of an interaction between discrete optical phonons and continuum carrier excitations in highly doped Ge. Moreover, Raman scattering is suppressed on the high wavenumber side of the peak, which is known as an anti-resonance. The anti-resonance is caused by destructive interference and is a characteristic of the Fano interference.<sup>55,57</sup>

## Electrical measurements

Transport characteristics such as resistivity ( $\rho$ ), carrier concentration, and Hall mobility ( $\mu_H$ ) of un-implanted and P-doped (after rFLA) samples were measured using van-der-Pauw geometry in the temperature range of 5 K to 300 K. As shown in Figure 4(a), the resistivity of all samples decreases at lower temperatures, which indicates a metallic behavior.

Moreover, Hall effect measurements indicate that the P-doped samples are successfully converted to n-type semiconductors (Figure S1). Temperature-dependent carrier concentration and Hall mobility are shown in Figures 4(b) and 4(c), respectively. The hole concentration of the un-implanted GeOI-0 sample is in the range of  $1.3 \times 10^{20} \text{ cm}^{-3}$ . The electron concentrations of the P-doped GeOI-1 and GeOI-2 samples after rFLA are in the range of

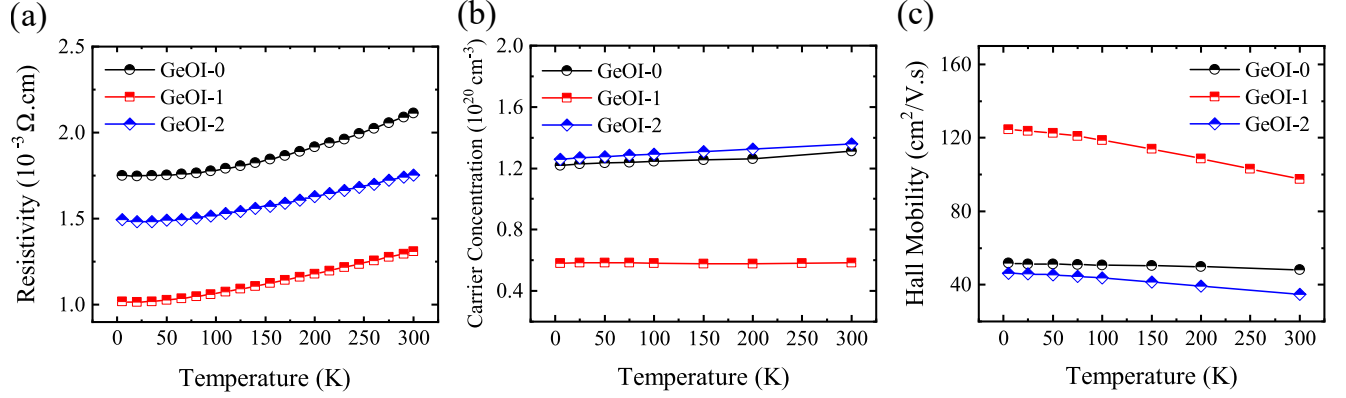


Figure 4: Temperature-dependent (a) resistivity( $\rho$ ), (b) carrier concentration, and (c) Hall mobility ( $\mu_H$ ) of the un-implanted (p-type) and P-implanted (n-type) samples after rFLA.

$5.8 \times 10^{19} \text{ cm}^{-3}$  and  $1.4 \times 10^{20} \text{ cm}^{-3}$ , respectively. Since the doping levels are so high, there is no freeze-out at low temperatures. The electron mobility in the GeOI-1 sample is in the range of  $100\text{-}120 \text{ cm}^2\text{V}^{-1}\text{s}^{-1}$ , which is higher than the carrier mobilities in the other samples. The GeOI-2 sample has higher electron concentration, leading to higher electron-impurity scattering, and hence, higher resistivity and lower mobility compared to the GeOI-1 sample.

## Characterization of n-type-doped GeNWs

### SEM and TEM analysis

Figure 5(a,b) shows the SEM images of the GeNW with an average width of 30 nm and the Hall-bar-configuration-based device of an n-type-doped GeNW with thin bars. TEM analysis was performed to investigate the nanostructure of the P-doped GeNWs after rFLA. Figure 6(a) shows a cross-sectional bright-field TEM image of a GeNW with an average width of 77 nm, obtained from the NW location indicated with a yellow dashed line in the SEM image shown in Figure 5. To record the TEM image, the specimen was oriented in Si  $[1 \bar{1} 0]$  zone axis geometry relative to the electron beam. Since the Ge on the  $\text{SiO}_2$  insulator is slightly misoriented with respect to the Si substrate, the TEM lamella had to be tilted by several degrees to bring the GeNW in  $[0 1 0]$  zone axis. The corresponding fast Fourier transform obtained from a high-resolution TEM image of the Ge region (not shown here)

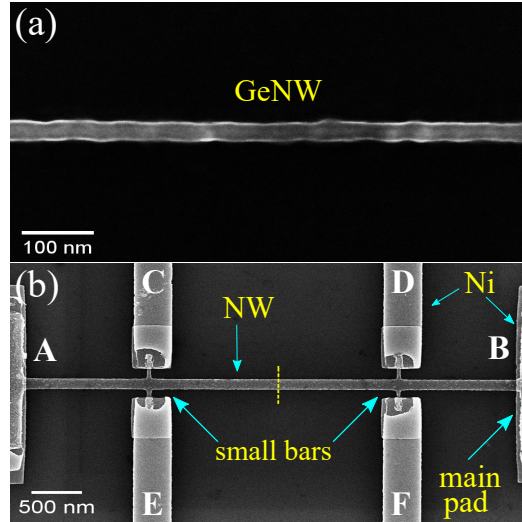


Figure 5: SEM images of (a) the GeNW with an average width of 30 nm, and (b) the Hall-bar-configuration-based device of an n-type-doped GeNW. The main pads (A,B) and the small bars (C-F) are shown in the image. The yellow dashed line refers to the NW location used for cross-sectional TEM analysis (Figure 6).

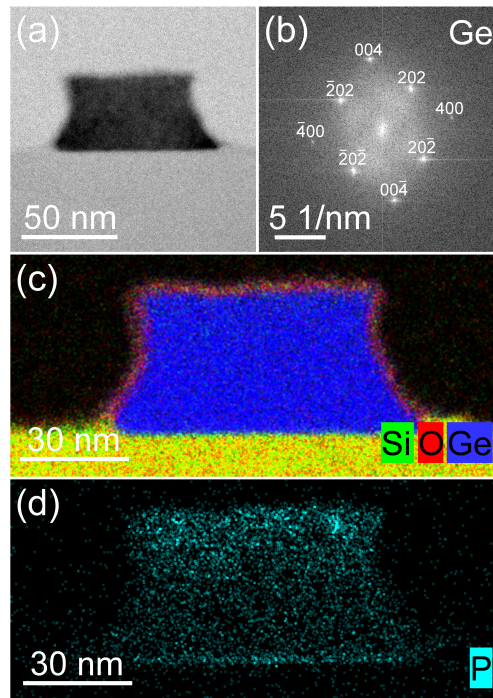


Figure 6: (a) Cross-sectional bright-field TEM image (obtained in Si  $[1\ 1\ 0]$  zone axis geometry) of a n-type-doped GeNW with an average width of 77 nm. (b) Fast Fourier transform of a high-resolution TEM image of the GeNW (obtained in Ge  $[0\ 1\ 0]$  zone axis geometry; not shown). (c) Superimposed Si (green), O (red), and Ge (blue) distributions as well as (d) P distribution (cyan) in the GeNW.

is depicted in Figure 6(b), leading to the conclusion that the P-doped GeNW has a single-crystalline structure. Regarding the chemical composition, Figures 6(c) and 6(d) display the superimposed Si, O, and Ge distributions and the P element map, respectively. As seen, P is not completely homogeneously distributed within the GeNW, which is in agreement with the SIMS results. There are slightly enhanced P signals in the upper third of the GeNW and at the interface with the SiO<sub>2</sub>. These results are confirmed by a longitudinal section of a GeNW region not covered with nickel, as shown in Figure S2.

A longitudinal view of the Ni contact area is shown in the bright-field TEM image of Figure 7(a). To further study the interface between Ni and Ge, spectrum imaging analysis based on EDXS was performed. As indicated by the slightly enhanced brightness of the upper GeNW part in the HAADF-STEM image in Figure 7(b) and confirmed by the Ni map in Figure 7(c), we observe Ni penetration into the GeNW to a depth of about 15 nm. While the Ge crystal structure seems to be unchanged in the deeper regions of this penetration zone, HRTEM imaging (Figure S3) points to the formation of a crystalline Ni germanide directly below the germanium oxide layer (black line in the HAADF-STEM image and the Ni map). Because of the small thickness of this discontinuous Ni germanide layer in combination with the finite thickness of the TEM lamella, Ni germanide phase determination was not possible. Above the oxide layer, there is an additional, about 2-nm-thick Ni-Ge intermixing layer. Regarding the P distribution within the GeNW (Figure 7(e)), there is no significant difference compared to the GeNW region without nickel (Figure S2).

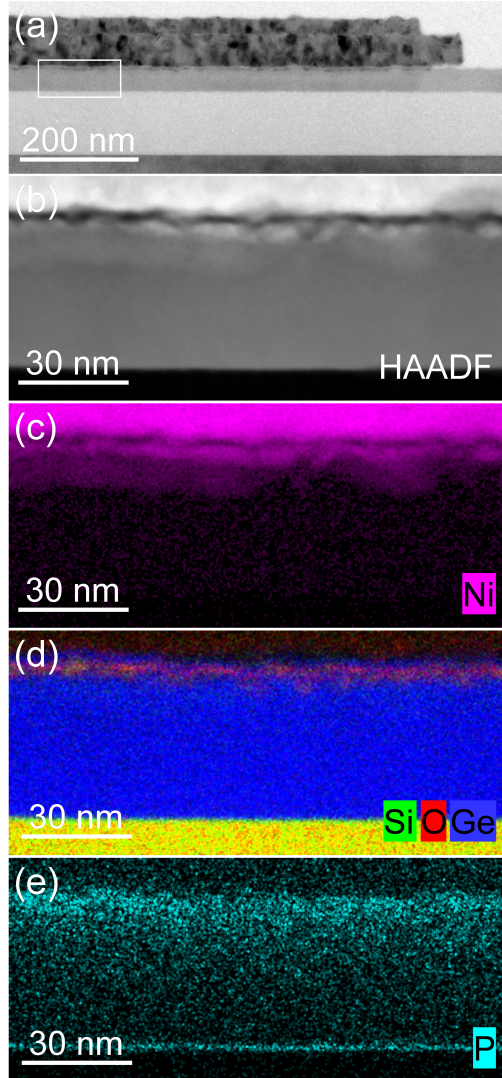


Figure 7: (a) Longitudinal bright-field TEM image (obtained in Si  $[1\ 1\ 0]$  zone axis geometry) of a n-type-doped GeNW region covered with Ni. (b) HAADF-STEM image, (c) Ni distribution (magenta), (d) superimposed Si (green), O (red), and Ge (blue) distributions as well as (e) P distribution (cyan) from the region marked with the white rectangle in panel (a).

### Electrical measurements

Two-probe measurements were performed on different contact pairs, called main pads and small bars, to investigate the linear characteristics of Ni contacts on the highly n-type-doped GeNWs with Hall bar configuration. The main pads refer to contacts AB and small bars refer to contacts CE or DF, shown in Figure 5. To perform the two-probe measurements,

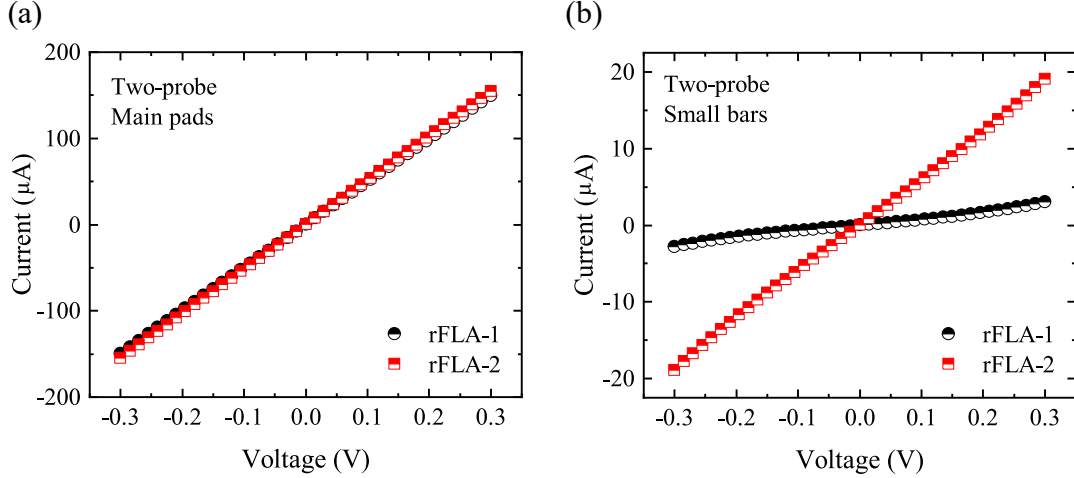


Figure 8: Two-probe measurements of (a) Ni-Ge main pads (contacts AB) and (b) Ni-Ge small bars (contacts CE) of n-type-doped GeNW with an average width of 77 nm. rFLA-1 refers to the first rFLA for activation of the P dopant atoms in the Ge layer, and rFLA-2 refers to the second rFLA for Ni germanide formation at the Ni-Ge contacts.

the voltage was swept through one contact while the other contact was grounded, and simultaneously the current was measured. As seen in Figure 8(a), two-probe current–voltage characteristics of the main pads exhibit linear behavior. However, the small bars (contacts CE) show a quasi-linear characteristic with a low conduction current (black circles in Figure 8(b)). Severe Fermi level pinning at the interface between Ni contacts and n-type Ge leads to the formation of a Schottky barrier, almost independent of the metal work function. Since the Schottky barrier width is inversely proportional to the doping density in semiconductors, the high carrier concentration shrinks the depletion region at the Ni-Ge interface, known as a tunnel junction, through which field emission can take place.<sup>27,30</sup> It seems that the carrier concentration in the small bars of GeNW with an average width of less than 50 nm is not high enough to shrink the Schottky barrier and show linear behavior. This might be related to the tendency of carriers to diffuse to the surface and get trapped at the surface states.<sup>58</sup> To improve the linear characteristics of the Ni contacts on the small bars of n-type-doped GeNWs, a second rear-side flash lamp annealing (rFLA-2) with an energy density of  $74 \text{ Jcm}^{-2}$  for 3 ms was conducted to form Ni germanide at the interface of the Ni-Ge contacts. As shown in Figure 8(b), the conduction current of the small bars increased

and became linear, which indicates the formation of Ni germanide at the interface of the Ni-Ge contacts. The formation of Ni germanide was confirmed by spectrum imaging analysis based on EDXS, although the Ni germanide phase was not possible to determine (Figure 7). Ni germanide has different phases including NiGe, Ni<sub>2</sub>Ge, Ni<sub>3</sub>Ge, and Ni<sub>5</sub>Ge<sub>3</sub>, whereby the stoichiometric NiGe phase forms at higher temperatures and has the lowest resistivity.<sup>30,59–63</sup>

The resistance of the n-type-doped GeNWs with different widths was determined using four-probe measurements. For each GeNW width, five devices were fabricated and characterized. To do so, the voltage drop along the GeNWs was measured via the contacts CF or DE while the current was sourced through the contacts AB. Figure 9(a) shows the four-probe current–voltage characteristics of the GeNW with an average width of 77 nm. As seen, the resistance of the GeNW decreased slightly after rFLA-2. The resistivity of the n-type-doped GeNWs was calculated using the measured resistance and the NW dimensions obtained via SEM images. The normalized resistivity of the n-type-doped GeNWs with respect to the thin film resistivity is plotted as a function of NW width at 300 K by considering the mean values and standard deviations, shown in Figure 9(b). The thin film resistivity was defined as the resistivity of the largest fabricated wire with a cross-section of 3000 nm × 38 nm, which is expected to behave similarly to a thin film.

The normalized resistivity of the GeNWs increases with decreasing NW width. According to the theoretical models of size-dependent electrical conductivity, the NW resistivity is mainly caused by a combination of three main carrier scattering mechanisms: background or bulk scattering, external surface scattering, and grain boundary scattering.<sup>64,65</sup> The HR-TEM analysis indicated that the P-doped GeNWs have a single-crystalline structure after recrystallization during rFLA. This means that the grain boundary scattering can be excluded. The increase of the surface-to-volume ratio of the small GeNWs leads to an enhanced contribution of surface scattering. Therefore, scattering in the region near the surface is the dominant mechanism for resistivity enhancement in the small GeNWs, which reduces the effective cross-section of the GeNWs. More details regarding the surface scattering region

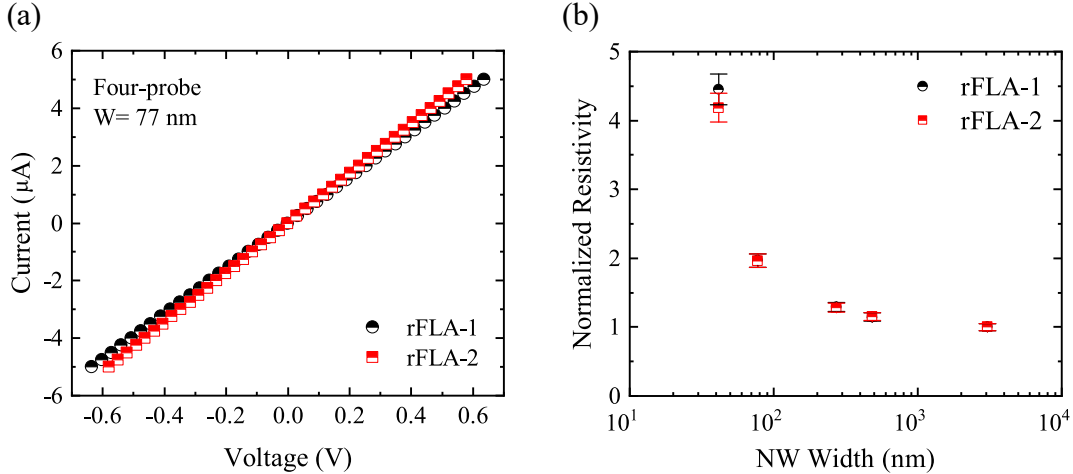


Figure 9: (a) Four-probe measurement of a GeNW with an average width of 77 nm. (b) Normalized resistivity of n-type-doped GeNWs as a function of NW width by considering the mean values and standard deviations. rFLA-1 refers to the first rFLA for activation of the P dopant atoms in the Ge layer, and rFLA-2 refers to the second rFLA for Ni germanide formation at the Ni-Ge contacts.

near the surface were discussed elsewhere.<sup>58</sup> The surface passivation of GeNWs with a high-quality oxide layer such as  $\text{Al}_2\text{O}_3$  and annealing in a  $\text{N}_2$  ambient can decrease the resistivity by reducing the interface states and terminating the dangling bonds (Figure S4).<sup>66</sup> As seen in Figure 9(b), the normalized resistivity of the n-type-doped GeNWs remained almost the same after rFLA-2 except for NWs with average widths less than 50 nm, where the resistivity decreased slightly after rFLA-2. The resistivity reduction can be related to the incorporation of more P atoms in the Ge matrix or a reduction of the defect concentration (Figure S5).

Hall effect measurements were performed for n-type-doped GeNWs after rFLA-2 at room temperature using the Hall bar configuration. Detailed measurements are provided in the Supporting information (Figure S6). The estimated carrier concentrations as a function of the NW width are presented in Figure 10(a). As it can be seen, the carrier concentration of the GeNWs decreases slightly by narrowing the NW width. This is related to the tendency of carriers to diffuse to the NW surface and be trapped at the GeNW/ $\text{GeO}_x$  interface states. These interface states act as carrier traps and lead to a depleted region close to the NW surface, resulting in reduced carrier concentrations.<sup>67</sup> The biggest wire, considered

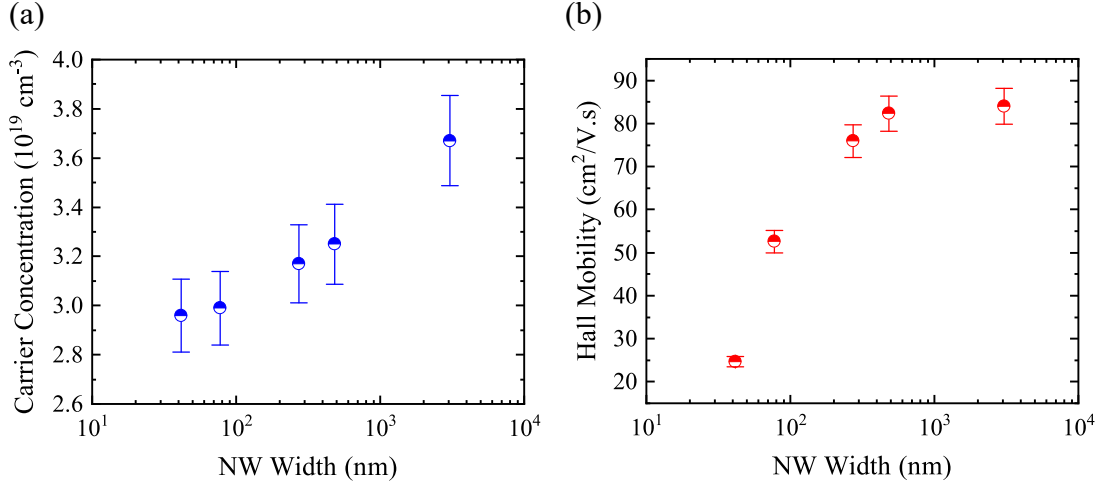


Figure 10: (a) Estimated carrier concentration and (b) Hall mobility of the n-type-doped GeNWs as a function of NW width by considering the mean values and standard deviations after rFLA-2 at room temperature.

in our manuscript, has a relatively large width of  $3 \mu\text{m}$  and we expect that by increasing further the wire width, the carrier concentration remains nearly the same. However, the carrier concentration of the widest wire, considered as a thin film, is about 36% lower than the one of the un-patterned sample (GeOI-1), measured by using van-der-Pauw geometry. This difference can be due to the different structures and different measurement methods. Because of the sample size, which can cause voltage shunting, the  $V_H$  measured with van-der-Pauw geometry is not as precise as the one measured by Hall bar configuration (Supporting Information). By having the carrier concentration and the resistivity ( $\rho$ ), the carrier Hall mobility ( $\mu_H$ ) of GeNWs can be determined. The room temperature Hall mobility of the n-type-doped GeNWs as a function of NW width is shown in Figure 10(b). As one can see, the carrier mobility drops with decreasing NW width. The reduced Hall mobility is related to the enhanced surface scattering of thin NWs because of their high surface-to-volume ratio, which leads to higher resistivity.

## Conclusions

In summary, ion beam implantation followed by rFLA was used to dope the Ge layer of a GeOI substrate with P atoms. The electrical characteristics of the GeOI substrates, measured via van-der-Pauw geometry, indicated that the P-doped Ge layers have a high electron concentration in the order of  $10^{19} - 10^{20} \text{ cm}^{-3}$ .

The highly n-type-doped GeNWs with different widths, fabricated using EBL and ICP-RIE, were characterized by using a Hall bar configuration. To overcome the Fermi level pinning, which leads to a formation of a Schottky barrier at the Ni-GeNWs contacts, a second rFLA for 3 ms was applied. According to TEM analysis, the rFLA caused the Ni diffusion into the Ge up to 15 nm, which improved the current-voltage characteristics because of the formation of Ni germanide at the Ni-GeNWs contacts. In addition, it was shown that with narrowing the NW width, the resistivity increases and the Hall mobility decreases, which is related to the enhanced carrier scattering near the NW surface and the decreased effective cross-sectional area of the GeNWs.

The presented combined approach of the fabrication of highly n-type-doped GeNWs in the p-type-doped Ge layers and their Ohmic contact formation can facilitate the construction of an axial p-n junction based on a single NW. The NW-based p-n junctions as a fundamental component can be used for electronic and optoelectronic devices.

## Acknowledgement

Support by the Nanofabrication Facilities Rossendorf (NanoFaRo) at the IBC is gratefully acknowledged. Authors would like to thank Dr. Ciaran Fowley for providing facilities in the Helmholtz-Zentrum Dresden-Rossendorf (HZDR) clean room. Also, Claudia Neisser and Tommy Schönherr are acknowledged for their instructions with conducting electron beam lithography and electron beam evaporation, as well as with operating the probe station for electrical measurements. Many thanks go to Ilona Skorupa for performing the metal deposi-

tion for unpatterned GeOI substrates and Annette Kunz for TEM lamella preparation. Also, the use of the HZDR Ion Beam Center TEM facilities, RBS, and ion implantation is gratefully acknowledged. Furthermore, the funding of TEM Talos by the German Federal Ministry of Education and Research (BMBF), Grant No. 03SF0451, in the framework of HEMCP is gratefully acknowledged. This work was partially financed by the Initiative and Networking Fund of the German Helmholtz Association through Helmholtz International Research School for Nanoelectronic Networks NanoNet (VH-KO-606) and by the Bundesministerium für Bildung und Forschung (BMBF) under the project "ForMikro": Group IV heterostructures for high performance nanoelectronic devices (SiGeSn NanoFETs) (Project-ID: 16ES1075). Also, this work was partially funded by SAB through the ESF Re-Learning project, SAB-Antragsnummer 100382146.

## Supporting Information Available

The following file is available free of charge.

- Supporting information: The calculation of the lattice parameters, additional experimental details, and graphs of Hall Effect measurements, TEM analysis, and Raman spectra of n-type-doped GeNWs (PDF)

## References

- (1) Goley, P. S.; Hudait, M. K. Germanium based field-effect transistors: Challenges and opportunities. *Materials* **2014**, *7*, 2301–2339.
- (2) Sgourou, E.; Panayiotatos, Y.; Vovk, R.; Kuganathan, N.; Chroneos, A. Diffusion and Dopant Activation in Germanium: Insights from Recent Experimental and Theoretical Results. *Applied Sciences* **2019**, *9*, 2454.

- (3) Tutuc, E.; Appenzeller, J.; Reuter, M. C.; Guha, S. Realization of a Linear Germanium Nanowire p–n Junction. *Nano Letters* **2006**, *6*, 2070–2074.
- (4) Sistani, M.; Staudinger, P.; Lugstein, A. Polarity Control in Ge Nanowires by Electronic Surface Doping. *The Journal of Physical Chemistry C* **2020**, *124*, 19858–19863.
- (5) John, J. W.; Dhyani, V.; Georgiev, Y. M.; Gangnaik, A. S.; Biswas, S.; Holmes, J. D.; Das, A. K.; Ray, S. K.; Das, S. Ultrahigh Negative Infrared Photoconductance in Highly As-Doped Germanium Nanowires Induced by Hot Electron Trapping. *ACS Applied Electronic Materials* **2020**, *2*, 1934–1942.
- (6) Zhang, S.; Hemesath, E. R.; Perea, D. E.; Wijaya, E.; Lensch-Falk, J. L.; Lauhon, L. J. Relative influence of surface states and bulk impurities on the electrical properties of Ge nanowires. *Nano Letters* **2009**, *9*, 3268–3274.
- (7) Prucnal, S.; Liu, F.; Voelskow, M.; Vines, L.; Rebohle, L.; Lang, D.; Berencén, Y.; Andric, S.; Boettger, R.; Helm, M.; Zhou, S.; Skorupa, W. Ultra-doped n-type germanium thin films for sensing in the mid-infrared. *Scientific Reports* **2016**, *6*, 27643.
- (8) Simoen, E.; Schaekers, M.; Liu, J.; Luo, J.; Zhao, C.; Barla, K.; Collaert, N. Defect engineering for shallow n-type junctions in germanium: Facts and fiction. *Physica Status Solidi (a)* **2016**, *213*, 2799–2808.
- (9) Kim, S.; Hill, D. J.; Pinion, C. W.; Christesen, J. D.; McBride, J. R.; Cahoon, J. F. Designing morphology in epitaxial silicon nanowires: the role of gold, surface chemistry, and phosphorus doping. *ACS Nano* **2017**, *11*, 4453–4462.
- (10) Seifner, M. S.; Sistani, M.; Porrati, F.; Di Prima, G.; Pertl, P.; Huth, M.; Lugstein, A.; Barth, S. Direct synthesis of hyperdoped germanium nanowires. *ACS Nano* **2018**, *12*, 1236–1241.

- (11) Ray, S. K.; Katiyar, A. K.; Raychaudhuri, A. K. One-dimensional Si/Ge nanowires and their heterostructures for multifunctional applications-a review. *Nanotechnology* **2017**, *28*, 092001.
- (12) Guilloy, K.; Pauc, N.; Gentile, P.; Robin, E.; Calvo, V. Uniform phosphorus doping of untapered germanium nanowires. *Nanotechnology* **2016**, *27*, 485701.
- (13) Tian, B.; Zheng, X.; Kempa, T. J.; Fang, Y.; Yu, N.; Yu, G.; Huang, J.; Lieber, C. M. Coaxial silicon nanowires as solar cells and nanoelectronic power sources. *Nature* **2007**, *449*, 885–889.
- (14) Yan, R.; Gargas, D.; Yang, P. Nanowire photonics. *Nature Photonics* **2009**, *3*, 569–576.
- (15) Park, C. J.; Jung, S. M.; Kim, J. H.; Shin, M. W. Conformal doping strategy for fin structures: tailoring of dopant profile through multiple monolayer doping and capping layer control. *Semiconductor Science and Technology* **2020**, *35*, 055028.
- (16) Duffy, R.; Shayesteh, M.; Thomas, K.; Pelucchi, E.; Yu, R.; Gangnaik, A.; Georgiev, Y. M.; Carolan, P.; Petkov, N.; Long, B.; Holmes, J. D. Access resistance reduction in Ge nanowires and substrates based on non-destructive gas-source dopant in-diffusion. *Journal of Materials Chemistry C* **2014**, *2*, 9248–9257.
- (17) Duffy, R.; Ricchio, A.; Murphy, R.; Maxwell, G.; Murphy, R.; Piaszenski, G.; Petkov, N.; Hydes, A.; O’Connell, D.; Lyons, C.; Kennedy, N.; Sheehan, B.; Schmidt, M.; Crupi, F.; Holmes, J. D.; Hurley, P. K.; Connolly, J.; Hatem, C.; Long, B. Diagnosis of phosphorus monolayer doping in silicon based on nanowire electrical characterisation. *Journal of Applied Physics* **2018**, *123*, 125701.
- (18) Long, B.; Verni, G. A.; O’Connell, J.; Shayesteh, M.; Gangnaik, A.; Georgiev, Y. M.; Carolan, P.; O’Connell, D.; Kuhn, K.; Clendenning, S. B.; Nagle, R.; Duffy, R.; Holmes, J. Doping top-down e-beam fabricated germanium nanowires using molecular monolayers. *Materials Science in Semiconductor Processing* **2017**, *62*, 196–200.

- (19) Berencén, Y.; Prucnal, S.; Möller, W.; Hübner, R.; Rebohle, L.; Schönherr, T.; Khan, M. B.; Wang, M.; Glaser, M.; Georgiev, Y.; Erbe, A.; Lugstein, A.; Helm, M.; Zhou, S. Formation of n- and p-type regions in individual Si/SiO<sub>2</sub> core/shell nanowires by ion beam doping. *Nanotechnology* **2018**, *29*, 474001.
- (20) Zhou, S. *Transition metal implanted ZnO: A correlation between structure and magnetism*; PhD thesis, TU Dresden; <https://nbn-resolving.org/urn:nbn:de:bsz:14-ds-1209998012687-36583>, 2008.
- (21) Prucnal, S.; Rebohle, L.; Skorupa, W. Doping by flash lamp annealing. *Materials Science in Semiconductor Processing* **2017**, *62*, 115–127.
- (22) Kittl, J.; Opsomer, K.; Torregiani, C.; Demeurisse, C.; Mertens, S.; Brunco, D.; Van Dal, M.; Lauwers, A. Silicides and germanides for nano-CMOS applications. *Materials Science and Engineering: B* **2008**, *154*, 144–154.
- (23) Chawanda, A.; Nyamhere, C.; Auret, F.; Mtangi, W.; Diale, M.; Nel, J. Thermal annealing behaviour of platinum, nickel and titanium Schottky barrier diodes on n-Ge (1 0 0). *Journal of Alloys and Compounds* **2010**, *492*, 649–655.
- (24) Martens, K.; Rooyackers, R.; Firrincieli, A.; Vincent, B.; Loo, R.; De Jaeger, B.; Meuris, M.; Favia, P.; Bender, H.; Douhard, B.; Vandervorst, W.; Simoen, E.; Jurczak, M.; Wouters, D. J.; Kittl, J. A. Contact resistivity and Fermi-level pinning in n-type Ge contacts with epitaxial Si-passivation. *Applied Physics Letters* **2011**, *98*, 013504.
- (25) Firrincieli, A.; Martens, K.; Rooyackers, R.; Vincent, B.; Rosseel, E.; Simoen, E.; Geypen, J.; Bender, H.; Claeys, C.; Kittl, J. Study of ohmic contacts to n-type Ge: Snowplow and laser activation. *Applied Physics Letters* **2011**, *99*, 242104.
- (26) Lieten, R.; Degroote, S.; Kuijk, M.; Borghs, G. Ohmic contact formation on n-type Ge. *Applied Physics Letters* **2008**, *92*, 022106.

- (27) Habanyama, A. *Advanced Material and Device Applications with Germanium*; BoD-Books on Demand, 2018.
- (28) Bardeen, J. Surface states and rectification at a metal semi-conductor contact. *Physical Review* **1947**, *71*, 717–727.
- (29) Sze, S.; Ng, K. K. *Physics of Semiconductor Devices*; John Wiley & Sons, 1981.
- (30) Gallacher, K.; Velha, P.; Paul, D. J.; MacLaren, I.; Myronov, M.; Leadley, D. R. Ohmic contacts to n-type germanium with low specific contact resistivity. *Applied Physics Letters* **2012**, *100*, 022113.
- (31) Zhou, Y.; Ogawa, M.; Han, X.; Wang, K. L. Alleviation of Fermi-level pinning effect on metal/germanium interface by insertion of an ultrathin aluminum oxide. *Applied Physics Letters* **2008**, *93*, 202105.
- (32) Lin, J. Y. J.; Roy, A. M.; Nainani, A.; Sun, Y.; Saraswat, K. C. Increase in current density for metal contacts to n-germanium by inserting TiO<sub>2</sub> interfacial layer to reduce Schottky barrier height. *Applied Physics Letters* **2011**, *98*, 092113.
- (33) Comrie, C.; Smeets, D.; Pondo, K.; Van der Walt, C.; Demeulemeester, J.; Knaepen, W.; Detavernier, C.; Habanyama, A.; Vantomme, A. Determination of the dominant diffusing species during nickel and palladium germanide formation. *Thin Solid Films* **2012**, *526*, 261–268.
- (34) Chilukusha, D.; Pineda-Vargas, C.; Nemitudi, R.; Habanyama, A.; Comrie, C. Micro-probe PIXE study of Ni–Ge interactions in lateral diffusion couples. *Nuclear Instruments and Methods in Physics Research Section B: Beam Interactions with Materials and Atoms* **2015**, *363*, 161–166.
- (35) Zheng, J.; Zhang, Y.; Liu, Z.; Zuo, Y.; Li, C.; Xue, C.; Cheng, B.; Wang, Q. Fabrication

- of low-resistance Ni ohmic contacts on  $n^+$ - $\text{Ge}_{1-x}\text{Sn}_x$ . *IEEE Transactions on Electron Devices* **2018**, *65*, 4971–4974.
- (36) Li, H.; Cheng, H.; Lee, L.; Lee, C.; Su, L.; Suen, Y. Electrical characteristics of Ni Ohmic contact on n-type GeSn. *Applied Physics Letters* **2014**, *104*, 241904.
- (37) Svensson, J.; Sourab, A. A.; Tarakanov, Y.; Lee, D. S.; Park, S. J.; Baek, S. J.; Park, Y. W.; Campbell, E. E. B. The dependence of the Schottky barrier height on carbon nanotube diameter for Pd–carbon nanotube contacts. *Nanotechnology* **2009**, *20*, 175204.
- (38) Alshareef, H. N.; Quevedo-Lopez, M.; Majhi, P. Contact materials for nanoelectronics. *MRS Bulletin* **2011**, *36*, 90–94.
- (39) Landman, U.; Barnett, R. N.; Scherbakov, A. G.; Avouris, P. Metal-semiconductor nanocontacts: silicon nanowires. *Physical Review Letters* **2000**, *85*, 1958–1961.
- (40) Sett, S.; Das, K.; Raychaudhuri, A. Investigation of factors affecting electrical contacts on single germanium nanowires. *Journal of Applied Physics* **2017**, *121*, 124503.
- (41) Chandra, N.; Tracy, C. J.; Cho, J. H.; Picraux, S.; Hathwar, R.; Goodnick, S. M. Vertically grown Ge nanowire Schottky diodes on Si and Ge substrates. *Journal of Applied Physics* **2015**, *118*, 024301.
- (42) El Hajraoui, K.; Robin, E.; Zeiner, C.; Lugstein, A.; Kodjikian, S.; Rouviere, J. L.; Den Hertog, M. In Situ Transmission Electron Microscopy Analysis of Copper–Germanium Nanowire Solid-State Reaction. *Nano Letters* **2019**, *19*, 8365–8371.
- (43) Luong, M. A.; Robin, E.; Pauc, N.; Gentile, P.; Sistani, M.; Lugstein, A.; Spies, M.; Fernandez, B.; Den Hertog, M. I. In-Situ Transmission Electron Microscopy Imaging of Aluminum Diffusion in Germanium Nanowires for the Fabrication of Sub-10 Nm Ge Quantum Disks. *ACS Applied Nano Materials* **2020**, *3*, 1891–1899.

- (44) Rebohle, L.; Prucnal, S.; Skorupa, W. A review of thermal processing in the subsecond range: semiconductors and beyond. *Semiconductor Science and Technology* **2016**, *31*, 103001.
- (45) Skorupa, W.; Schumann, T.; Rebohle, L. Millisecond thermal processing using flash lamps for the advancement of thin layers and functional coatings. *Surface and Coatings Technology* **2017**, *314*, 169–176.
- (46) Loup, V.; Gabette, L.; Roure, M. C.; Kachtouli, R.; Jourdan, M.; Besson, P.; Petitdier, S. Si and SiGe Alloys Wet Etching Using TMAH Chemistry. *ECS Transactions* **2013**, *58*, 47–55.
- (47) Namatsu, H.; Yamaguchi, T.; Nagase, M.; Yamazaki, K.; Kurihara, K. Nano-patterning of a hydrogen silsesquioxane resist with reduced linewidth fluctuations. *Microelectronic Engineering* **1998**, *41*, 331–334.
- (48) Georgiev, Y. M.; Henschel, W.; Fuchs, A.; Kurz, H. Surface roughness of hydrogen silsesquioxane as a negative tone electron beam resist. *Vacuum* **2005**, *77*, 117–123.
- (49) Mirza, M. M.; Zhou, H.; Velha, P.; Li, X.; Docherty, K. E.; Samarelli, A.; Ternent, G.; Paul, D. J. Nanofabrication of high aspect ratio (50:1) sub-10 nm silicon nanowires using inductively coupled plasma etching. *Journal of Vacuum Science & Technology B, Nanotechnology and Microelectronics: Materials, Processing, Measurement, and Phenomena* **2012**, *30*, 06FF02.
- (50) Gangnaik, A. S.; Georgiev, Y. M.; Collins, G.; Holmes, J. D. Novel germanium surface modification for sub-10 nm patterning with electron beam lithography and hydrogen silsesquioxane resist. *Journal of Vacuum Science & Technology B, Nanotechnology and Microelectronics: Materials, Processing, Measurement, and Phenomena* **2016**, *34*, 041603.

- (51) Henschel, W.; Georgiev, Y. M.; Kurz, H. Study of a high contrast process for hydrogen silsesquioxane as a negative tone electron beam resist. *Journal of Vacuum Science & Technology B: Microelectronics and Nanometer Structures Processing, Measurement, and Phenomena* **2003**, *21*, 2018–2025.
- (52) Cheng, R.; Wang, W.; Gong, X.; Sun, L.; Guo, P.; Hu, H.; Shen, Z.; Han, G.; Yeo, Y. C. Relaxed and strained patterned germanium-tin structures: a Raman scattering study. *ECS Journal of Solid State Science and Technology* **2013**, *2*, P138–P145.
- (53) Xu, C.; Senaratne, C. L.; Kouvetakis, J.; Menendez, J. Experimental doping dependence of the lattice parameter in n-type Ge: Identifying the correct theoretical framework by comparison with Si. *Physical Review B* **2016**, *93*, 041201.
- (54) Prucnal, S.; Berencén, Y.; Wang, M.; Grenzer, J.; Voelskow, M.; Hübner, R.; Yamamoto, Y.; Scheit, A.; Bärwolf, F.; Zviagin, V.; Schmidt Grund, R.; Grundmann, M.; Zuk, J.; Turek, M.; Drozdziel, A.; Pyszniak, K.; Kudrawiec, R.; Polak, M. P.; Rebohle, L.; Skorupa, W.; Helm, M.; Zhou, S. Strain and band-gap engineering in Ge-Sn alloys via P doping. *Physical Review Applied* **2018**, *10*, 064055.
- (55) Fukata, N.; Sato, K.; Mitome, M.; Bando, Y.; Sekiguchi, T.; Kirkham, M.; Hong, J. i.; Wang, Z. L.; Snyder, R. L. Doping and Raman characterization of boron and phosphorus atoms in germanium nanowires. *ACS Nano* **2010**, *4*, 3807–3816.
- (56) D’Costa, V. R.; Tolle, J.; Poweleit, C. D.; Kouvetakis, J.; Menéndez, J. Compositional dependence of Raman frequencies in ternary  $\text{Ge}_{1-x-y}\text{Si}_x\text{Sn}_y$  alloys. *Physical review B* **2007**, *76*, 035211.
- (57) Yogi, P.; Saxena, S. K.; Mishra, S.; Rai, H. M.; Late, R.; Kumar, V.; Joshi, B.; Sagdeo, P. R.; Kumar, R. Interplay between phonon confinement and Fano effect on Raman line shape for semiconductor nanostructures: Analytical study. *Solid State Communications* **2016**, *230*, 25–29.

- (58) Echresh, A.; Arora, H.; Fuchs, F.; Li, Z.; Hübner, R.; Prucnal, S.; Schuster, J.; Zahn, P.; Helm, M.; Zhou, S.; Erbe, A.; Rebohle, L.; Georgiev, Y. M. Electrical Characterization of Germanium Nanowires Using a Symmetric Hall Bar Configuration: Size and Shape Dependence. *Nanomaterials* **2021**, *11*, 2917.
- (59) Begeza, V.; Mehner, E.; Stöcker, H.; Xie, Y.; García, A.; Hübner, R.; Erb, D.; Zhou, S.; Rebohle, L. Formation of Thin NiGe Films by Magnetron Sputtering and Flash Lamp Annealing. *Nanomaterials* **2020**, *10*, 648.
- (60) Prucnal, S.; Frigerio, J.; Napolitani, E.; Ballabio, A.; Berencén, Y.; Rebohle, L.; Wang, M.; Böttger, R.; Voelskow, M.; Isella, G.; Hübner, R.; Manfred, H.; Zhou, S.; Skorupa, W. In situ ohmic contact formation for n-type Ge via non-equilibrium processing. *Semiconductor Science and Technology* **2017**, *32*, 115006.
- (61) Tang, J.; Wang, C. Y.; Xiu, F.; Zhou, Y.; Chen, L. J.; Wang, K. L. Formation and device application of Ge nanowire heterostructures via rapid thermal annealing. *Advances in Materials Science and Engineering* **2011**, *2011*, 6316513.
- (62) Tang, J.; Wang, C. Y.; Xiu, F.; Hong, A. J.; Chen, S.; Wang, M.; Zeng, C.; Yang, H. J.; Tuan, H. Y.; Tsai, C. J.; Chen, L. J.; Wang, K. L. Single-crystalline Ni<sub>2</sub>Ge/Ge/Ni<sub>2</sub>Ge nanowire heterostructure transistors. *Nanotechnology* **2010**, *21*, 505704.
- (63) Tang, J.; Wang, C. Y.; Xiu, F.; Lang, M.; Chu, L. W.; Tsai, C. J.; Chueh, Y. L.; Chen, L. J.; Wang, K. L. Oxide-confined formation of germanium nanowire heterostructures for high-performance transistors. *ACS Nano* **2011**, *5*, 6008–6015.
- (64) Li, R.; Mi, L.; Wang, J.; Mao, M.; Gu, W.; Zhu, Y. Conductivity Size Effect of Square Cross-Section Polycrystalline Nanowires. *Materials* **2019**, *12*, 2129.
- (65) Xue, W.; Gu, W. Conductivity size effect of polycrystalline metal nanowires. *AIP Advances* **2016**, *6*, 115001.

- (66) Simanullang, M.; Usami, K.; Noguchi, T.; Surawijaya, A.; Kodera, T.; Kawano, Y.; Oda, S. Surface passivation of germanium nanowires using Al<sub>2</sub>O<sub>3</sub> and HfO<sub>2</sub> deposited via atomic layer deposition technique. *Japanese Journal of Applied Physics* **2014**, *53*, 06JG04.
- (67) Ou, X.; Kanungo, P. D.; Kogler, R.; Werner, P.; Gosele, U.; Skorupa, W.; Wang, X. Carrier profiling of individual Si nanowires by scanning spreading resistance microscopy. *Nano Letters* **2010**, *10*, 171–175.

# TOC Graphic

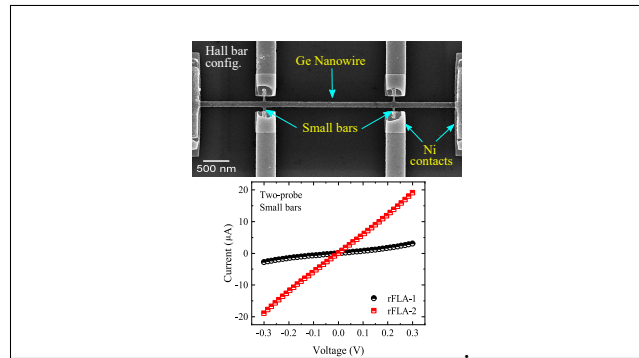


Figure 11